JOURNAL OF PROPULSION AND POWER
Vol. 15, No. 5, September–October 1999

Surface Pressure Measurements in Supersonic Transverse Injection Flowfields

M. R. Gruber*
U.S. Air Force Research Laboratory, Wright–Patterson Air Force Base, Ohio 45433
and
L. P. Goss†
Innovative Scientific Solutions, Inc., Dayton, Ohio 45440

Pressure-sensitive paint (PSP) was used to examine the surface pressures in flowfields created by the transverse injection of air through circular and elliptic nozzles into a supersonic freestream. Four jet-to-freestream momentum flux ratios J were investigated for each nozzle. A comparison of the PSP results with conventional pressure measurements indicates good agreement between the two techniques. Results confirm that operating conditions and injector geometry significantly affect the surface pressure field around a transverse jet. Increases in J alter the wall pressure field upstream and downstream of the injector. Injector geometry strongly affects the upstream extent of the separation region and the bow shock, and the character of the wake region downstream of the jet. Also, the effective back pressures computed from the PSP data for the elliptic injector cases are significantly higher than for the circular injector cases, presenting a possible explanation for recently observed differences in transverse penetration.

Nomenclature

A_{xs}	= cross-sectional area
a	= semimajor axis, 3.18 mm for circular, 6.25 mm for elliptic
b	= semiminor axis, 3.18 mm for circular, 1.63 mm for elliptic
d_{eff}	= effective diameter, $2(A_{xs}/\pi)^{1/2}$, 6.35 mm for circular and elliptic
I	= luminescence
J	= jet-to-freestream momentum flux ratio, $(\gamma p M^2)_j/(\gamma p M^2)_\infty$
K_q	= Stern–Volmer constant
M	= Mach number
P_{O_2}	= partial pressure of oxygen
p	= pressure
p_{eb}	= effective back pressure
T	= temperature
x, y, z	= streamwise, transverse, and spanwise coordinates
γ	= specific heat ratio
δ	= boundary-layer thickness
ϵ	= eccentricity $[1 - (b/a)^2]^{1/2}$, 0 for circular, 0.97 for elliptic
θ	= angular coordinate, 0 deg at leading edge of injector orifice

Subscripts

j	= jet exit property
o	= stagnation condition, condition without oxygen present
ref	= reference
2	= property behind a normal shock
∞	= freestream property

Received 3 February 1998; revision received 5 January 1999; accepted for publication 15 January 1999.

*Aerospace Engineer, Propulsion Sciences and Advanced Concepts Division, High Speed Systems Development Branch, Building 18, 1790 Loop Road North. Senior Member AIAA.

†President, 2786 Indian Ripple Road. Member AIAA.

Introduction

EFFECTIVE injection into a supersonic flow remains a daunting task in the successful design and implementation of a hydrocarbon-fueled scramjet combustor. Rapid mixing between the fuel and air is required while total pressure loss must be minimized. Additionally, heat loads to the wall must remain within the structural constraints of the combustor material. One possible fuel-delivery scheme for scramjet combustors involves normal injection into a supersonic crossflow. A schematic of the flowfield around a single circular injector appears in Fig. 1. As shown in the illustration, a three-dimensional bow shock forms upstream of the injector exit. This shock interacts with the approaching boundary layer, resulting in separation. Another separated region forms just downstream of the injector. Transverse injection provides rapid fuel penetration into the crossflow and promotes relatively rapid near-field mixing. However, this design can introduce large total pressure losses and significant wall heating effects.

Transverse injection into a supersonic crossflow has been the subject of several experimental and computational studies.[1–15] Recent studies[10–13] demonstrate the effectiveness of modifying the injector geometry from circular to elliptic. These experiments showed that a gaseous jet issuing from an elliptic nozzle performs better in terms of mixing, total pressure loss, and lateral spreading than a jet from a circular nozzle of the same effective diameter operating at the same relative conditions. It was also shown that the separated region upstream of the injector was smaller at the jet centerline in the elliptic case. However, the transverse penetration in the elliptic case was ~20% less than in the circular case at the same jet-to-freestream momentum flux ratio. Schetz and Billig[1] pointed to a parameter called the effective back pressure as an important indicator of the extent of jet penetration into the crossflow. This pressure is the average static pressure in the near-field region around the injector, analogous to the back pressure for the case of injection into a quiescent medium.[16] It is expected that injector geometry strongly influences the near-field static pressure distribution. Thus, the effective back pressure may describe the observed penetration differences.

Wall static pressures have been commonly measured[4,9,15] and predicted[5,6,8] in many transverse injection studies. Generally, in the case of a single three-dimensional circular injector placed in the wall, the static pressure distribution has been measured using pressure taps arranged along the streamwise direction at the spanwise centerline of the injector. Many numerical studies of this important

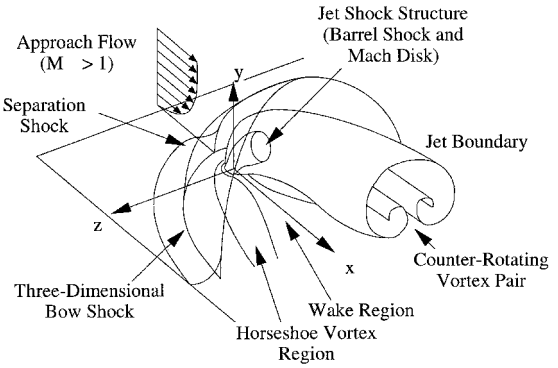

Fig. 1 Perspective view of the mean transverse injection flowfield.

fluid dynamic problem have been two dimensional; i.e., slot injection. Those that do simulate a three-dimensional flowfield focus mainly on the spanwise centerline of the injector. As such, most work presented to date provides information at the time-averaged symmetry plane of the flowfield. Because the jet/crossflow interaction has been shown to be highly three dimensional, it is imperative to obtain static pressure data from around the injector orifice as well. Without such information, the effective back pressure cannot be estimated. Recently, Everett et al.[15] studied the surface pressure field around a single circular injector for three momentum flux ratios using pressure-sensitive paint (PSP). Many features of the flowfield were observed, including the increasing shock strength with increasing J and the locations of the maximum and minimum pressures upstream and downstream of the injector. The authors also captured the circumferential variation of the pressure field and computed a value of the effective back pressure using the following expression (assuming spanwise symmetry):

$$\frac{p_{\text{eb}}}{p_2} = \frac{1}{\pi}\frac{1}{p_2}\int_0^{\pi} p(\theta)\,\mathrm{d}\theta \tag{1}$$

A linear relationship between p_{eb} and J for the case of a circular injector was obtained.[15] The correlation between p_{eb} and p_2 agreed closely with earlier results.[7]

The objective of this work is to obtain a more thorough understanding of the performance differences between gaseous injection into a supersonic crossflow through circular and elliptic injectors. As noted previously, effective back pressure and jet-to-freestream momentum flux ratio are parameters that describe the transverse penetration of gaseous jets into a supersonic crossflow. For the case of the elliptic injector, a suppression of penetration has been observed compared with injection through a circular nozzle at an identical momentum flux ratio.[11] Thus, the wall static pressure field around the two orifices is of significant interest as it applies to the determination of the effective back pressure. In this study, PSP is used to experimentally determine the surface pressure field around two wall-mounted injectors. This technique allows examinations of the wall pressure field with improved spatial resolution over conventional pressure taps. Also, the two-dimensional images can be analyzed for qualitative and quantitative features of the flowfield at the wall.

Experimental Facility and Diagnostics

The transverse injection experiments discussed next were performed in the supersonic research facility located at Wright–Patterson Air Force Base. The major highlights of this facility appear in the following section; further details may be found elsewhere.[17] The injector geometries are then presented, followed by discussions of the PSP technique and its application.

Flow Facility

A continuous supply of pressurized air enters the inlet section of the test apparatus and flows into a settling chamber. This section houses flow-conditioning devices and sensors for measuring the stagnation pressure and temperature of the freestream. The air is then accelerated in a two-dimensional nozzle section by a pair of nozzle blocks producing a nominally Mach 2 freestream. This supersonic flow then enters a constant area test section (cross section dimensions of 131 × 152 mm). Several fused silica windows placed in the test section walls allow for nonintrusive investigations of the flowfield.

Injectors

Two injector geometries were incorporated into the test section. Details of the injectors appear elsewhere[10,11]; the Nomenclature section summarizes their geometric features. Each injector was placed at the same streamwise location to ensure that the approaching turbulent boundary layer would be of the same thickness ($\sim\delta/d_{\text{eff}} = 1$). The elliptic injector was oriented with its major axis nominally aligned with the crossflow direction. In fabricating the elliptic injector, its alignment was found to be ~10-deg skew to the approach flow. Each injector had a pressure tap for setting the jet exit static pressure; stagnation temperature was measured in the injectant supply line. Three pressure taps were placed on the spanwise centerline at locations $x/d_{\text{eff}} = 5$, 8, and 11 from each jet centerline.

The various pressure taps were connected to a Pressure Systems Incorporated (PSI) 8400 system. This device has 16-bit resolution and ±0.05% full-scale (25, 100, and 500 psig) accuracy. For each channel, an average of 100 instantaneous pressure measurements was recorded. A Mensor 14500 DPGII digital barometer provided daily atmospheric pressure readings. A Pentium 133-MHz computer, running custom data-acquisition software, acquired the pressure data from the PSI system and the barometer for later analysis.

PSP Technique

The PSP technique offers several advantages over conventional pressure taps. The locations of the taps are generally predetermined during the design phase of an experiment, making optimum placement difficult. An additional complication arises due to the finite volume required for the tap itself and often precludes placing enough taps in the particular region to adequately resolve pressure gradients. Measuring pressures using PSP effectively eliminates these disadvantages; it can be applied to most surfaces and can provide nearly limitless spatial resolution. Other references are available for more details in addition to those that are presented next.[18]

In PSP, a probe molecule is promoted to an excited state by absorbing a photon of appropriate energy. Photoluminescence is one mechanism by which the molecule can lose the excess energy and return to the ground state. For pressure-sensitive coatings, the excess energy can also be absorbed by oxygen molecules through dynamic quenching. Oxygen quenching is usually modeled by some variation of the Stern–Volmer relation. In its simplest form, the relation is given by

$$I_o/I = 1 + K_q P_{\text{O}_2} \tag{2}$$

Unfortunately, the pressure-sensitive probe molecules have other mechanisms by which they can return to the ground state that are manifested in a sensitivity to temperature. To apply the Stern–Volmer model, the luminescence intensity at a reference pressure level must be divided by the luminescence intensity at some test condition over the area of interest. For this method, the ratio of luminescence intensities is calibrated to indicate surface pressure. The intensities are generally sampled over an area using a charge-coupled device (CCD) camera.

The pressure paint used in this study was pyrene in a silicone binder (Dow Corning 734). The silicone is a low molecular weight conformal coating, making it ideal for pressure-paint applications. This paint, when excited in the uv, emits in the visible between 400–500 nm. The pyrene paint displays strong monomer and excimer emissions that are both pressure sensitive. Pyrene's fluorescence lifetime is very short (300 ns under vacuum), making it relatively insensitive to its thermal environment.

The pyrene–silicone mixture was sprayed directly onto each clean injector model and allowed to dry/cure for 2–3 h. As each injector was painted, an aluminum sample was also painted for calibration

purposes. The full temperature and pressure calibrations of the paints were carried out in a rig prior to transverse injection experiments. The calibration rig was specially designed to allow computer control of the thermodynamic conditions. The rig operates over a 243–423-K temperature range and a 0–200-kPa pressure range. The Stern–Volmer calibration curve for the paint is shown for a temperature of 295 K in Fig. 2. Temperature effects are illustrated in Fig. 3. In this plot, the pressure is shown as a function of temperature for a given I_{ref}/I ratio. An increase in surface temperature of 5 K results in a pressure decrease of about 4 kPa. The temperature sensitivity of the paint also appears in Fig. 3 (~0.8 kPa/K). Because the stainless-steel test section used in this investigation operates at steady-state conditions and injection durations are short, no appreciable surface temperature variation is expected (<10 K).

PSP Imaging System and Data Analysis

A pulsed nitrogen laser (Photon Technology International, model GL-3300) provided the necessary excitation source for the probe molecule in the PSP; i.e., 337 nm. This laser was remotely triggered using an HP 8112A pulse generator. Laser light was transmitted to the injector block using a fiber-optic cable, allowing precise illumination of the injector model. A PixelVision back-illuminated CCD camera was used to collect the fluorescence from the PSP. The camera controller interfaced to a Pentium personal computer running the PixelView software package. Laser and camera pulses were monitored using a LeCroy 9314L oscilloscope.

Data acquisition consisted of taking background images (10); wind-off images (10); vacuum images (where the test section was maintained between 14 and 20 kPa, 10); wind-on images at four different injector pressure (20); and postrun wind-off images (10). The analysis of the PSP images consisted of several steps. First, the images in the various ensembles were averaged. Then, the average background was subtracted from each of the averaged wind-on and wind-off images. Next, the wind-on images were image-shifted to ensure good overlap with the wind-off images (typical shifts of 0.5 pixel along rows and columns). The resulting wind-on images were then divided into the wind-off images, and these ratioed images were finally converted to pressure by applying the calibration data obtained in the static rig.

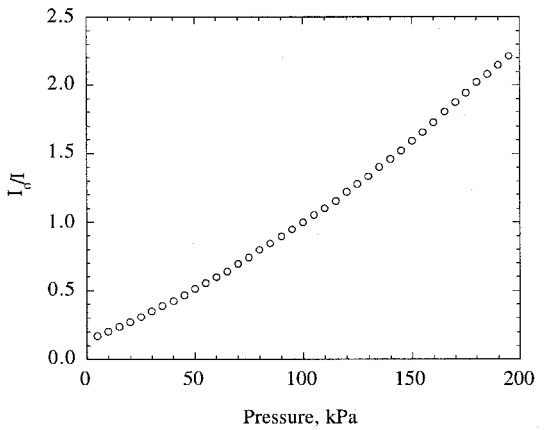

Fig. 2 Calibration curve for pyrene-based pressure paint obtained at 295 K.

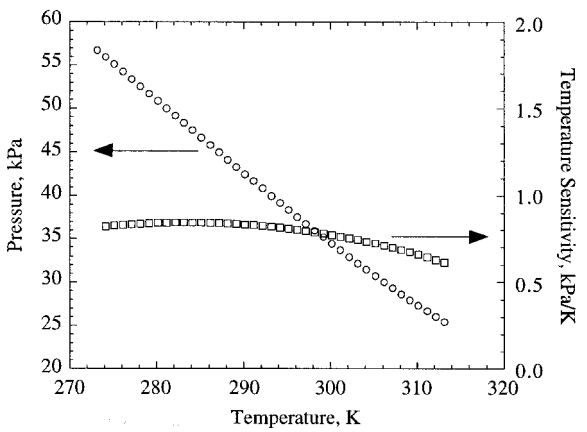

Fig. 3 Apparent pressure and temperature sensitivity for pyrene-based pressure paint.

Results and Discussion

The conditions of the approaching freestream air were $M_\infty = 1.95$, $p_{o,\infty} = 319 \pm 1$ kPa, and $T_{o,\infty} = 297 \pm 3$ K. Conditions for the injection cases studied in this investigation appear in Table 1; air injection through circular and elliptic nozzles appear as cases C1–C4 and E1–E4, respectively. The following sections present the results obtained in this investigation. Representative PSP images from the injection cases are presented first, followed by centerline pressure profiles and comparisons between conventional and PSP pressure data. The wake region is then discussed, followed by results of the effective back-pressure analysis.

PSP Images

Figures 4 and 5 show the ensemble-averaged PSP results as color images of the near-field region around the selected injector geometries. The data contained in each of these images have only been normalized by the freestream static pressure, and the appropriate color bar has been placed beneath each image. Regions of normalized static pressure greater than unity are displayed as light blue/green/yellow/red, whereas normalized pressure zones below unity appear dark blue/purple. A contour of $p/p_\infty = 0.7$ appears in each image. The freestream flow direction is from bottom to top and the jet fluid flows out of the paper. The physical dimensions of the displayed regions are ~79 mm (x) × 80 mm (z). Each pixel in the displayed region is 0.187 mm.[2] The pressure taps machined in the hardware for these experiments are roughly 0.75 mm in diameter (noted in Figs. 4a and 5a).

Circular Injector

Figures 4a–4d present the PSP images obtained for cases C1–C4, respectively. The region upstream of the injector exit displays two locally high values of the normalized wall static pressure p/p_∞. The first zone occurs well upstream and represents the separation region. As J increases, this zone moves farther upstream in the images. A second high-pressure zone occurs just ahead of the injector exit. This region results from the pressure rise across the bow shock wave. With increasing J, this region grows in size and wraps around the windward side of the injector and the peak pressures within this zone increase. For example, the spanwise extent of the $p/p_\infty = 1.7$ contour increases from ~$1.7d_{\text{eff}}$ in case C1 to $3.7d_{\text{eff}}$ in case C4.

Another region of interest occurs directly downstream of the injector exit. Here, the freestream flow expands around the injector until it separates, resulting in a low-pressure wake. Farther downstream, the flow recompresses back to the freestream static pressure. As J increases, the wake region grows in both its streamwise and spanwise extents. Also, the recompression process requires a longer streamwise distance for completion. For example, the downstream extent of the $p/p_\infty = 0.7$ contour increases from ~$x/d_{\text{eff}} = 2.2$ in

Table 1 Experimental conditions

Case	p_j, kPa	$T_{o,j}$, K	J
C1	164.6 ± 0.2	297 ± 3	0.99
C2	328.2 ± 0.2	297 ± 3	1.97
C3	496.1 ± 0.7	297 ± 3	2.98
C4	658.0 ± 0.4	297 ± 3	3.95
E1	160.8 ± 0.2	297 ± 3	0.96
E2	329.7 ± 0.5	297 ± 3	1.97
E3	494.4 ± 0.8	297 ± 3	2.95
E4	661.8 ± 0.8	297 ± 3	3.94

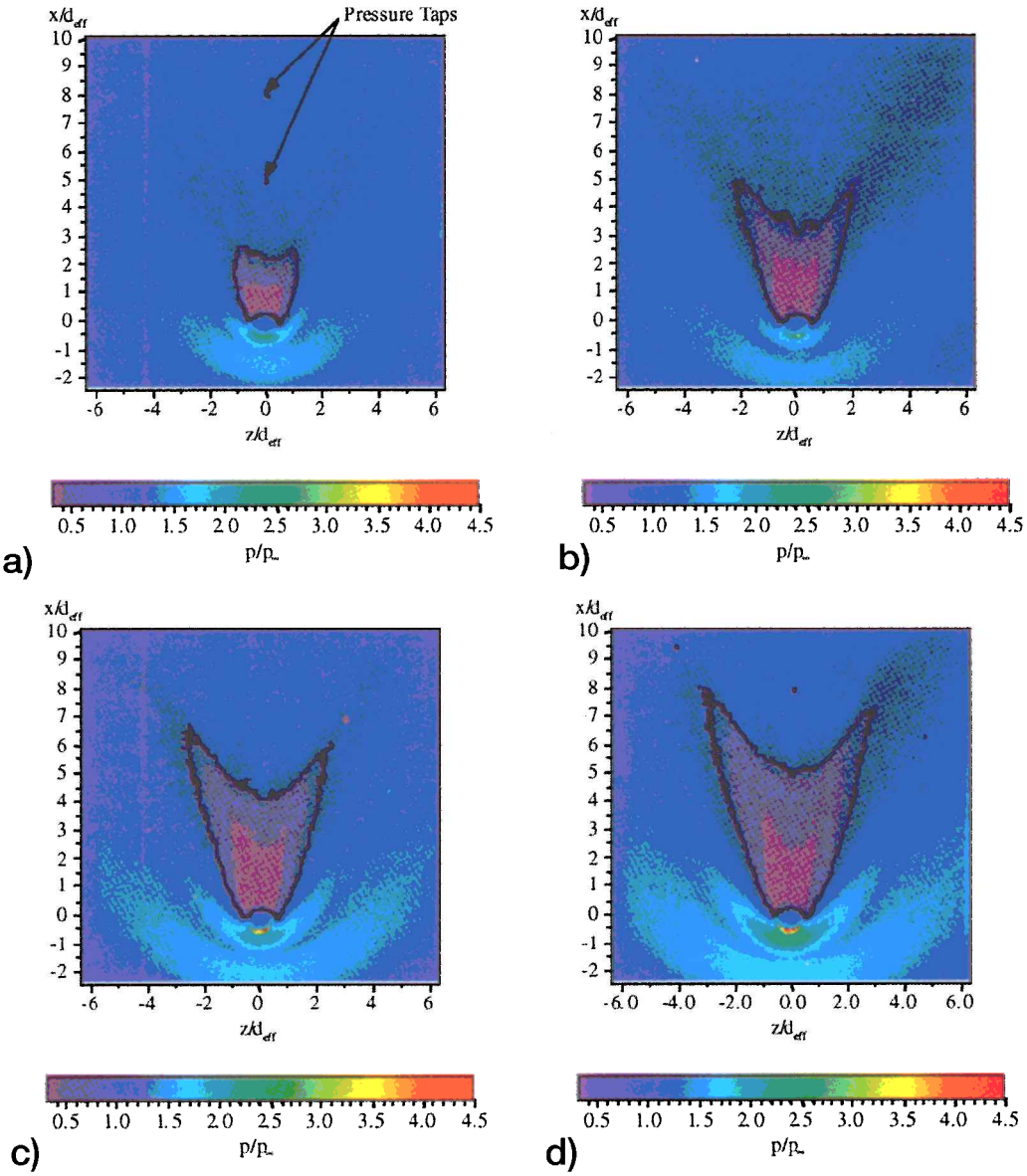

Fig. 4 Normalized PSP images, circular injector. Case a) C1, b) C2, c) C3, and d) C4.

case C1 to $x/d_{\text{eff}} = 5.0$ in case C4, whereas the spanwise spread increases from $2.3d_{\text{eff}}$ in case C1 to $5.7d_{\text{eff}}$ in case C4. These results compare well with those of Everett et al.[15]

Elliptic Injector

Figures 5a–5d present the PSP images obtained for cases E1–E4, respectively. These images appear very similar in many respects to those shown in Fig. 4 for the circular injector. However, some very interesting differences are apparent. The region upstream of the injector exit remains dominated by two locally high-pressure zones; i.e., the upstream separation zone and the bow shock. However, the separation region appears smaller at the spanwise centerline of the injector and the bow shock occurs closer to the upstream edge of the injector in cases E1–E4. The trends observed as J increases are similar to those mentioned earlier in that both the extent of the high-pressure region just behind the bow shock and the bow shock strength increase. Also, the separated region occurs farther upstream as J increases. These results agree with those from a previous investigation.[12]

In cases E1–E4, the wake appears narrower very near the leeward edge of the injector than in C1–C4, and it remains narrower until the recompression region. For comparison, the spanwise extent of the $p/p_\infty = 0.7$ contour is $\sim 1.8d_{\text{eff}}$ for case E1 and $4.6d_{\text{eff}}$ for case E4. These values are ~20% smaller than the respective data from the circular injector. Beyond this location, the wake spreads rapidly in the spanwise direction. The streamwise distances required for recompression in these cases (measured from the injector centerline) are essentially equal to those from the circular injector cases ($x/d_{\text{eff}} = 2.1$ for case E1 and 5.0 for case E4). Another feature of the wake region in the elliptic injection cases is the locally high-pressure zone on the injector centerline just downstream of the recompression line.

Centerline Pressure Profiles

Figures 6a–6d present the centerline PSP and conventional pressure data obtained from the circular and elliptic injection flowfields. In these figures, PSP results are shown as line plots, whereas open symbols indicate conventional measurements. The PSP results agree with the conventionally measured pressures within 5–10%. This agreement was obtained assuming an isothermal temperature for the test section. This indicates that the pyrene-based pressure paint is relatively insensitive to temperature effects. No in situ,[19,20] K-fit,[21] or temperature-correction[22] calibrations were necessary to obtain this agreement for these test conditions.

Circular Injector

Figure 6a shows the centerline static pressure profile obtained for case C1. Two regions of relatively high static pressure appear. The

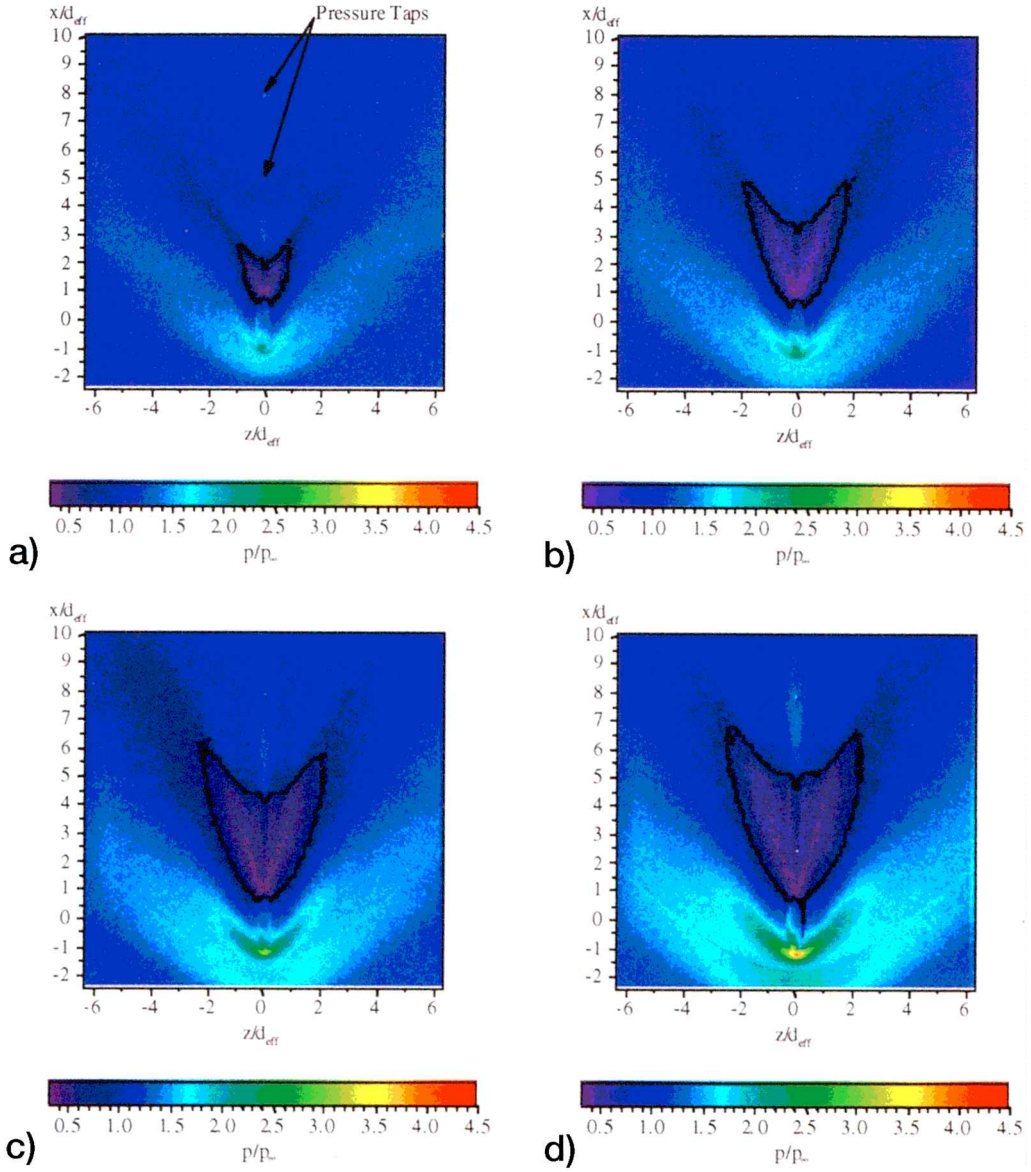

Fig. 5 Normalized PSP images, elliptic injector. Case a) E1, b) E2, c) E3, and d) E4.

first region begins upstream of $x/d_{\text{eff}} = -2$ and corresponds to the separation zone ahead of the injector. The second region corresponds to the bow shock wave and occurs suddenly at approximately one effective diameter upstream of the streamwise jet centerline. The region immediately downstream of the injector is dominated by extremely low pressures. Farther downstream, the flow along the wall is gradually recompressed until it reaches the freestream static pressure.

Figures 6b–6d present the pressure results obtained from the PSP images as J is increased (cases C2, C3, and C4, respectively). Increases in J result in the separation region and the bow shock locations being forced upstream. The pressure downstream of the bow shock also steadily increases with increasing J. This agrees with the results of recent visualization studies,[11,12,15] and suggests that the bow shock strength increases with J. The low-pressure wake region becomes increasingly more prominent as J increases. This region gradually grows toward the downstream direction requiring a longer distance for recompression. It should also be noted that the recompression wave strengthens with increasing J, often resulting in a slight overcorrection where the pressure in the wake is higher than the freestream static pressure.

Elliptic Injector

The centerline pressure distribution for case E1 appears in Fig. 6a. As with case C1, two regions of relatively high static pressure appear in this profile upstream of the injector exit. The first region corresponds to the separation zone ahead of the injector. It begins at about the same spatial location as in case C1. The second high-pressure region, i.e., the bow shock, however, occurs suddenly at just over one effective diameter upstream of the streamwise jet centerline. This suggests that the separation region ahead of the elliptic injector is smaller compared with that of the circular injector for similar operating conditions. The pressure rise across the bow shock is also observed to be smaller for the elliptic injection flowfield as compared with case C1. Thus, it is reasonable to say that the bow shock occurring in case E1 is somewhat weaker than the corresponding feature from case C1. These results agree with those of an earlier study.[12]

The pressure data downstream of the injector exit are of particular interest. Compared with the values measured in case C1, the wake in case E1 has a similar minimum pressure level. However, the recompression process occurring in the elliptic injector flowfield is very rapid and strong compared with the circular case. This is shown in Fig. 6a by the large rise in pressure at approximately $x/d_{\text{eff}} = 3$. It is thought that the axis-switch occurring in the elliptic injector flowfield[11] creates relatively strong axial vorticity, which acts to entrain more freestream fluid into the wake, thereby resulting in this rapid rise in static pressure on the centerline. Once the peak centerline pressure has been reached, the flow expands to the freestream static pressure.

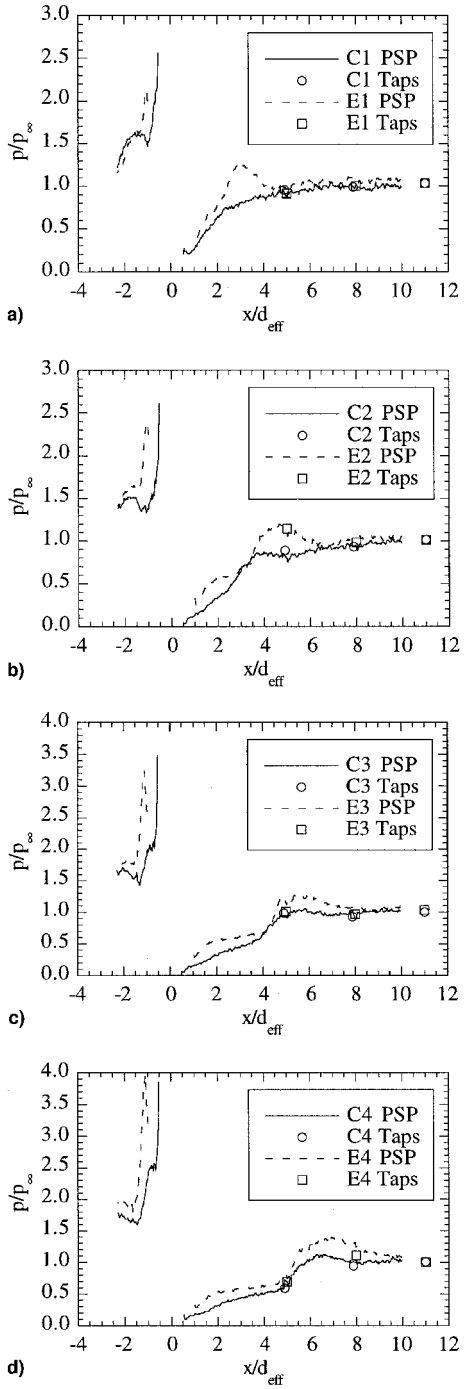

Fig. 6 Centerline pressure data from PSP images and pressure. J = a) 1, b) 2, c) 3, and d) 4.

Figures 6b–6d present the centerline pressure profiles obtained for cases E2–E4, respectively. These figures continue to illustrate the main features observed in Fig. 6a. The upstream separation region in the elliptic injector flowfield is somewhat smaller in streamwise extent than in the circular injector flowfield. The bow shock remains slightly weaker until the highest momentum flux ratio case. The wake has predominantly higher pressures immediately downstream of the elliptic injector, and it recompresses rapidly to relatively higher peak pressures. Additionally, several trends are common to those observed in the circular cases as J increases. These include the stronger bow shock occurring farther upstream and the longer distance required for full wake recompression back to the freestream static pressure.

Wake Pressure Profiles

Figures 7 and 8 show normalized static pressure profiles taken from the PSP images for the two injectors. These profiles are plotted in such a way as to examine the development of the wake between streamwise locations $x/d_{\text{eff}} = 1$ and 8. Each plot has broken lines that correspond to both the streamwise position of the profile and the $p/p_\infty = 1$ level. Thus, areas of the plotted profiles above the broken line indicate $p/p_\infty > 1$, whereas areas below the broken line show $p/p_\infty < 1$.

Circular Injector

Figure 7a presents the normalized wake pressure profiles for case C1. As suggested by the image in Fig. 4a, the wake behind the circular injector for this case dominates the region near the injector.

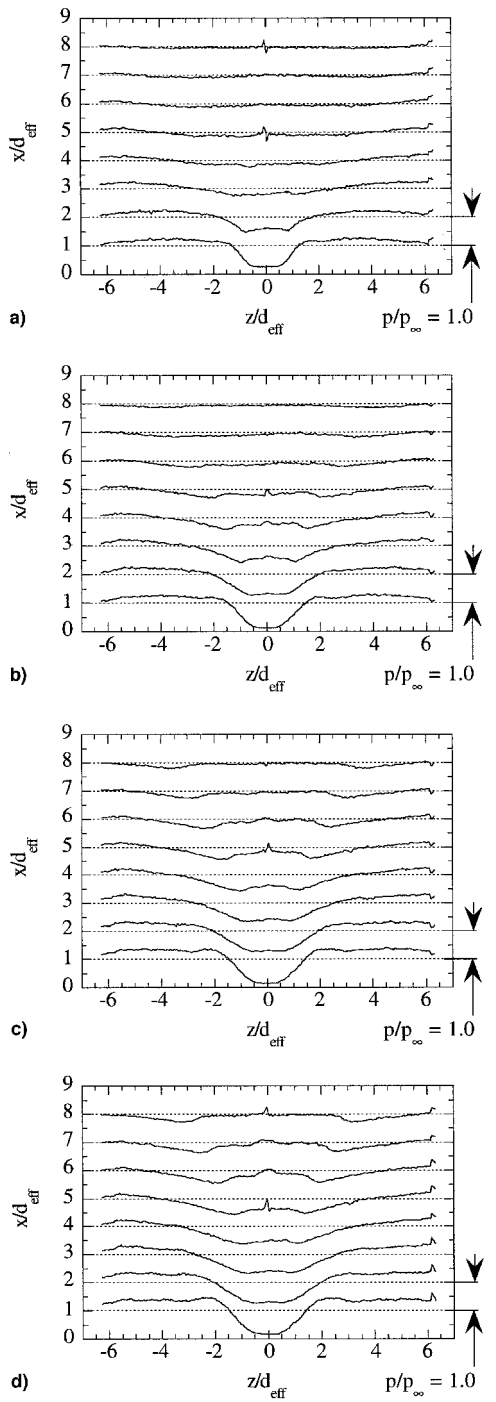

Fig. 7 Normalized static pressure profiles in the wake region of the circular injector. Case a) C1, b) C2, c) C3, and d) C4.

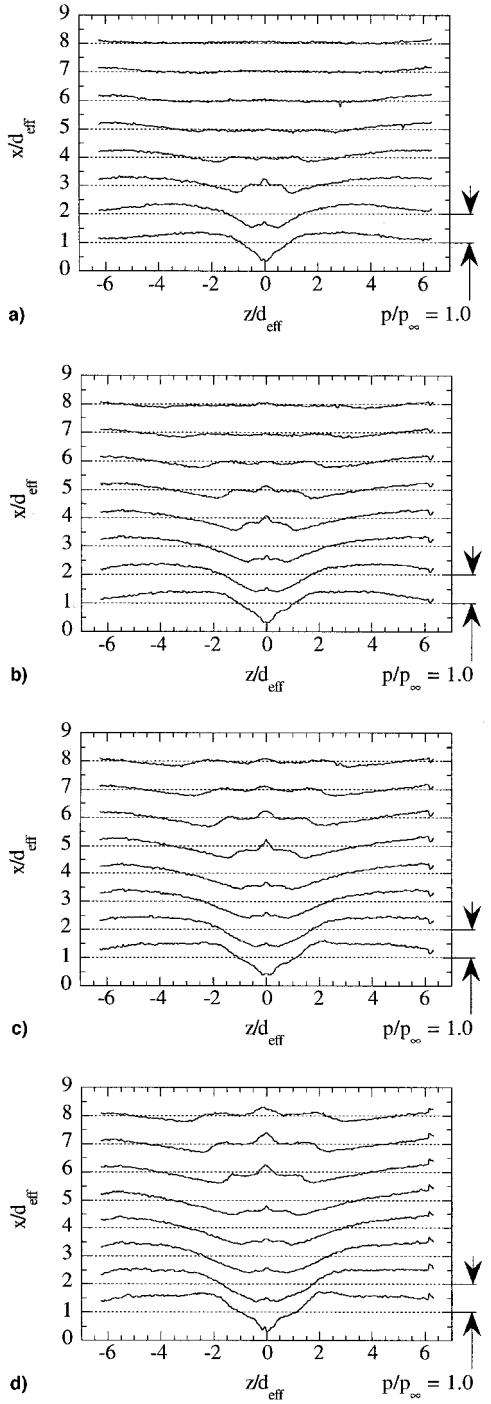

Fig. 8 Normalized static pressure profiles in the wake region of the elliptic injector. Case a) E1, b) E2, c) E3, and d) E4.

The influence of the three-dimensional bow shock and separation regions are also observed in the profile taken from $x/d_{\text{eff}} = 1$, as areas where $p/p_\infty > 1$. The recompression process begins between $x/d_{\text{eff}} = 1$ and 2, as indicated by the curvature change in the pressure profile near the spanwise centerline. This process continues until approximately $x/d_{\text{eff}} = 4$ or 5, where the entire region downstream of the injector has reached $p/p_\infty = 1$. Two discontinuities appear in the profiles obtained from five and eight effective diameters downstream; these correspond to the static pressure taps on the injector wall. It should be noted that all of the profiles presented indicate the central region of the wake having $p/p_\infty \leq 1$.

As J increases, the character of the wake changes significantly. Figures 7b–7d show the normalized pressure profiles obtained for cases C2–C4, respectively. One of the principal effects of increasing J is a longer distance required to complete the recompression process. For example, in Fig. 7d, two depressed regions remain in the $x/d_{\text{eff}} = 8$ profile. These correspond to the "wings" of the wake and are clearly observed in the image shown in Fig. 4d. However, the central wake region has reached $p/p_\infty = 1$ by approximately $x/d_{\text{eff}} = 7$. Also, the start of the recompression process in the central region of the wake generally moves downstream with increasing J (between two and three effective diameters by case C4). Another effect of increasing J is that the influence of the high-pressure regions that wrap around the injector become stronger. The high normalized pressure regions to either side of the core of the wake gradually grow in extent from Figs. 4a to 4d.

Elliptic Injector

Figure 8a presents the normalized pressure profiles from the wake region of case E1. These are similar in many respects to those from Fig. 7a for case C1, although there are also several important differences. The low-pressure wake is very prominent in the two profiles at $x/d_{\text{eff}} = 1$ and 2. Also, the recompression process begins somewhere between these two locations, as suggested by the sharp change in curvature at the spanwise centerline. However, this process appears to be significantly stronger in case E1 than in case C1. Evidence for this exists in the profile from $x/d_{\text{eff}} = 3$, where the normalized pressure at the spanwise centerline suddenly increases above unity. Downstream of this location, the wake is essentially at a constant pressure equal to the freestream static pressure. Another significant difference observed in case E1 compared with case C1 is the width of the wake near the injector. For the case of the elliptic injector, the wake region is very narrow. This characteristic continues as the wake develops.

The profiles taken from cases E2–E4 appear in Figs. 8b–8d, respectively. As observed in the circular injector flowfield, one of the effects of increasing J is to delay the complete recompression of the wake. This is clearly observed in Figs. 8b–8d. The wings of the wake are nearly as prominent in these plots as in Figs. 7b–7d for the circular injector. However, these features occur nearer to the spanwise centerline in the elliptic cases. The relatively strong recompression process is also observed in Figs. 8b–8d. In several of these profiles, the normalized pressure at the spanwise centerline of the wake is significantly greater than unity. The influence of the high-pressure regions resulting from the three-dimensional bow shock and separation regions are increasingly more prominent with larger values of J. For instance, compare the profiles from $x/d_{\text{eff}} = 1$ for cases E1 and E4 (Figs. 8a and 8d). The gradient between the lowest pressure in the wake and the highest pressure just outside the wake increases rapidly. It also increases above that observed in the circular injector flowfields. Thus, the rapid and strong recompression process that occurs in the elliptic injector flowfield may be fueled by this pressure difference. Also, the axis-switch that occurs in the elliptic injector flowfield[11] may contribute to the rapid recompression of the wake by enhancing the strength of the streamwise vortices and increasing their ability to entrain freestream fluid toward the centerline of the wake. This observation is consistent with recent results that show better mixing in the wake region behind an elliptic injector as compared with a circular injector.[11]

Effective Back Pressure Analysis

To compute the effective back-pressure values, a circumferential pressure contour was obtained from each PSP image. For the circular injector, the diameter of this contour was selected to be 1.5 times the injector diameter to avoid the influences of surface imperfections near the sharp injector exit. For the elliptic nozzle, an elliptic contour was chosen with semimajor and semiminor axes equal to 1.5 times those of the injector. Then, a region about each injector was expanded by a factor of 4 using bilinear interpolation. The spanwise coordinates locating the desired surface pressures were computed using each streamwise coordinate in the enlarged image and the equations describing a circle and an ellipse. Then, knowing the pixel location corresponding to the center of the injector exit, the angle θ was calculated.

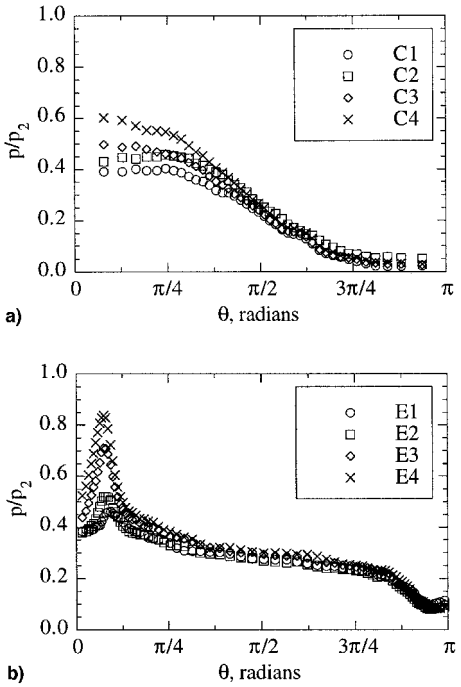

Fig. 9 Circumferential pressure distributions: a) circular and b) elliptic injectors.

Figure 9a presents the circumferential pressure distributions obtained from the four circular injection cases. The data presented are normalized by the static pressure that would occur downstream of a normal shock at the freestream conditions of this study. These plots show the gradual pressure increase upstream of the injector with increasing J. They also show that the expansion around the injector is essentially the same for all values of J. This observation is consistent with the results of Everett et al.[15] However, the magnitudes of the circumferential pressures in the present study are somewhat lower than in Ref. 15. It is thought that this disagreement results from the larger contour diameter used in this investigation.

The results from the elliptic injector appear in Fig. 9b. These distributions are quite different from those shown in Fig. 9a for the circular injector. They indicate a gradual increase in pressure upstream of the injector with increasing J. It is also apparent that the expansion around the injector is essentially identical for all values of J studied. However, the similarities between the two sets of distributions stop at that point. The profiles shown in Fig. 9b exhibit a sharp peak just beyond the $\theta = 0$ rad location. It is suspected that the location of this peak results from the skewness resulting from the machining of the injector block; i.e., if machined perfectly, the peak would occur at $\theta = 0$ rad. The expansion around the injector is quite rapid, leading to a region of nearly constant pressure from $\theta = \pi/4$ to $3\pi/4$ rad. Finally, the expansion process resumes into the wake region behind the injector.

Once the circumferential pressure distributions are obtained, the effective back pressure may be computed using Eq. (1). The results of this calculation appear in Fig. 10. Again, the magnitudes of the computed effective back pressure in the present circular injection cases are somewhat lower than those shown in Everett et al.[15] However, the present results are of the same order of magnitude and show the same weak dependence on J. The results obtained from the elliptic injection cases also demonstrate a weak dependence on J. The error bars included in Fig. 10 represent the uncertainty associated with a nonisothermal wall ($\Delta T = 10$ K).

The most important result found in Fig. 10 is that the effective back pressures for the elliptic injection cases are all between 20 and 35% larger than their respective circular injection results. Thus, the elliptic jet encounters a relatively higher pressure environment than does the circular jet at the same operating conditions. It is therefore reasonable to expect that the elliptic jet will not penetrate as far into the crossflow as the circular jet. This analysis provides strong support for the recently observed differences in performance between these two injectors. It also supports the importance of the effective back-pressure concept as it applies to comparisons in transverse penetration performance between injectors of different geometry.

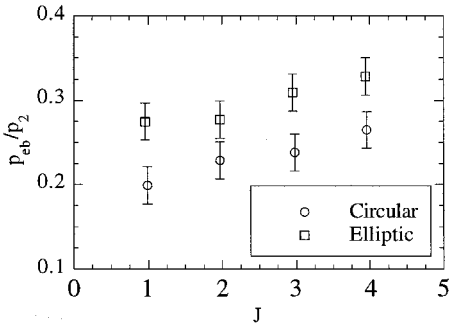

Fig. 10 Effects of J and injector geometry on effective back pressure.

Summary and Conclusions

PSP was used to examine the surface pressures in flowfields generated by the transverse injection of air through circular and elliptic nozzles into a supersonic freestream. Four jet-to-freestream momentum flux ratios were investigated for each jet. Images of the surfaces provide well-resolved representations of the flow around the injectors. Two dominant high-pressure regions exist upstream of the injectors corresponding to the separation and bow shock locations. These regions are highly three dimensional and wrap directly around the injector exit. The footprint of the bow shock is observed as the jet-to-freestream momentum flux ratio increases. The wake region downstream of the injector is characterized by very low static pressures. As the flow develops, it experiences recompression back toward the freestream static pressure. This region grows as the jet-to-freestream momentum flux ratio increases.

A comparison of the PSP results with conventional pressure measurements indicates good agreement (within 5–10%) between the two with no special treatment of the paint data. Results further show that jet operating conditions and injector geometry significantly affect the surface pressure field around a transverse jet. Increases in jet-to-freestream momentum flux ratio dramatically alter the wall pressure field upstream and downstream of the injector. Injector geometry strongly affects the upstream extent of the separation region and the bow shock, and the character of the wake region downstream of the jet. The elliptic jet flowfield has a markedly narrower wake region that often experiences a faster and stronger recompression process than the circular jet flowfield. Generally, normalized centerline wake pressures are higher in the elliptic injector flowfield. Also, the effective back pressures computed from the PSP data for the elliptic injector cases are significantly higher than for the circular injector cases, presenting a possible explanation for recently observed differences in transverse penetration.

Acknowledgments

This work was funded by the U.S. Air Force under Contract F33615-96-C-2638. The authors acknowledge the efforts of R. Fuller, K. Grinstead, K. Navarra, D. Trump, D. Schommer, and W. Terry for their assistance in the data acquisition and facility operation.

References

[1]Schetz, J. A., and Billig, F. S., "Penetration of Gaseous Jets Injected into a Supersonic Stream," *Journal of Spacecraft and Rockets*, Vol. 3, No. 11, 1966, pp. 1658–1665.

[2]Orth, R. C., and Funk, J. A., "An Experimental and Comparative Study of Jet Penetration in Supersonic Flow," *Journal of Spacecraft and Rockets*, Vol. 4, No. 9, 1967, pp. 1236–1242.

[3]Schetz, J. A., Hawkins, P. F., and Lehman, H., "Structure of Highly Underexpanded Transverse Jets in a Supersonic Stream," *AIAA Journal*, Vol. 5, No. 5, 1967, pp. 882–884.

[4]Spaid, F. W., and Zukoski, E. E., "A Study of the Interaction of Gaseous Jets from Transverse Slots with Supersonic External Flows," *AIAA Journal*, Vol. 6, No. 2, 1968, pp. 205–212.

[5]Fujimori, T., Kawai, M., Ikeda, H., Ando, Y., Ohmori, Y., Aso, S., and Fukuda, M., "Numerical Predictions of Two and Three Dimensional Sonic Gas Transverse Injections into Supersonic Crossflow," AIAA Paper 91-0415, Jan. 1991.

[6]Rizzetta, D. P., "Numerical Simulation of Slot Injection into a Turbulent Supersonic Stream," *AIAA Journal*, Vol. 30, No. 10, 1992, pp. 2434–2439.

[7]Papamoschou, D., and Hubbard, D. G., "Visual Observations of Supersonic Transverse Jets," *Experiments in Fluids*, Vol. 14, No. 6, 1993, pp. 468–476.

[8]Gerlinger, P., Algermissen, J., and Brüggemann, D., "Simulation of Turbulent Slot Injection of Different Gases into a Supersonic Airstream," AIAA Paper 94-2247, June 1994.

[9]Aso, S., Tannou, M., Maekawa, S., Okuyama, S., Ando, Y., Yamane, Y., and Fukuda, M., "A Study on Mixing Phenomena in Three-Dimensional Supersonic Flow with Circular Injection," AIAA Paper 94-0707, Jan. 1994.

[10]Gruber, M. R., Nejad, A. S., Chen, T. H., and Dutton, J. C., "Mixing and Penetration Studies of Sonic Jets in a Mach 2 Freestream," *Journal of Propulsion and Power*, Vol. 11, No. 2, 1995, pp. 315–323.

[11]Gruber, M. R., Nejad, A. S., and Dutton, J. C., "An Experimental Investigation of Transverse Injection from Circular and Elliptical Nozzles into a Supersonic Crossflow," Wright Lab., WL-TR-96-2102, Wright–Patterson AFB, OH, Jan. 1996.

[12]Gruber, M. R., Nejad, A. S., Chen, T. H., and Dutton, J. C., "Bow Shock/Jet Interaction in Compressible Transverse Injection Flowfields," *AIAA Journal*, Vol. 34, No. 10, 1996, pp. 2191–2193.

[13]Gruber, M. R., Nejad, A. S., Chen, T. H., and Dutton, J. C., "Large Structure Convection Velocity Measurements in Compressible Transverse Injection Flowfields," *Experiments in Fluids*, Vol. 22, No. 5, 1997, pp. 397–407.

[14]Gruber, M. R., Nejad, A. S., Chen, T. H., and Dutton, J. C., "Compressibility Effects in Supersonic Transverse Injection Flowfields," *Physics of Fluids*, Vol. 9, No. 5, 1997, pp. 1448–1461.

[15]Everett, D. E., Woodmansee, M. A., Dutton, J. C., and Morris, M. J., "Wall Pressure Measurements for a Sonic Jet Injected Transversely into a Supersonic Crossflow," *Journal of Propulsion and Power*, Vol. 14, No. 6, 1998, pp. 861–868.

[16]Adamson, T. C., and Nicholls, J. A., "On the Structure of Jets from Highly Underexpanded Nozzles into Still Air," *Journal of the Aero/Space Sciences*, Vol. 26, No. 1, 1959, pp. 16–24.

[17]Gruber, M. R., and Nejad, A. S., "New Supersonic Combustion Research Facility," *Journal of Propulsion and Power*, Vol. 11, No. 5, 1995, pp. 1080–1083.

[18]Crites, R., *Pressure Sensitive Paint Technique*, Lecture Series on Measurement Techniques, von Kármán Inst. of Fluid Dynamics, Rhode–Saint-Genese, Belgium, 1993.

[19]McLachlan, B., Kavandi, J., Callis, J., Gouterman, M., Green, E., Khalil, G., and Burns, D., "Surface Pressure Field Mapping Using Luminescent Coatings," *Experiments in Fluids*, Vol. 14, No. 1, 1993, pp. 33–41.

[20]McLachlan, B., Bell, J., Park, H., Kennelly, R., Schreiner, J., Smith, S., Strong, J., Gallery, J., and Gouterman, M., "Pressure-Sensitive Paint Measurements on a Supersonic High-Sweep Oblique Wing Model," *Journal of Aircraft*, Vol. 32, No. 2, 1995, pp. 217–224.

[21]Woodmansee, M. A., and Dutton, J. C., "Methods for Treating Temperature-Sensitivity Effects of Pressure-Sensitive Paints," AIAA Paper 97-0387, Jan. 1997.

[22]Morris, M. J., and Donovan, J. F., "Application of Pressure- and Temperature-Sensitive Paints to High-Speed Flows," AIAA Paper 94-2231, June 1994.

Color reproductions courtesy of U.S. Air Force Research Laboratory.